Adaptive Model Predictive Control for *LCL*-Filter Grid-Tied Inverters

Hasan Zamani, Karim Abbaszadeh, Mohammad Hadi Karimi, and Johan Gyselinck, *Member, IEEE*

***Abstract*—This article proposes adaptive continuous-control-set model predictive control (CCS-MPC) for three-phase *LCL*-filter grid-tied inverters in the stationary frame. The proposed control provides stability against the *LCL*-filter resonance and removes the need for active damping or passive damping. Furthermore, it can track sinusoidal references in the stationary frame close to zero offsets. Inductance variation of a grid is a challenging issue, which can shift the *LCL*-filter resonance. Even though CCS-MPC generally has good stability for parameter mismatches, the control is optimized for the nominal value of the parameters. A relatively large variation may deteriorate the performance of the control and cause instability in the closed-loop system. To solve this problem, the concept of CCS-MPC is developed to work with a variety of the grid-inductance changes. The controller coefficients are chosen with a sensitivity analysis to provide enough gain margins and phase margins for the whole interval of the presumption grid-inductance variation. Also, this selection guarantees the control robustness against mismatches of the *LCL*-filter capacitance and inductance. The real-time computation of advanced controllers is a challenging issue. The computation burden of the proposed CCS-MPC is mostly performed offline and just some simple numerical expression is executed in real time. Thus, it does not require a powerful but expensive processor for implementation. The simulation and experimental results prove the performance of the proposed controller for handling the *LCL*-filter resonance, grid-inductance variations, and tracking sinusoidal references.**

***Index Terms*—Computation time, continuous-control-set model predictive control (CCS-MPC), inherent robustness, *LCL*-filter resonance, sinusoidal references, steady-state offset.**

I. Introduction

GRID-TIED inverters deliver power from renewable energy sources to power grids and have attracted attention in recent years [1]. Usually, an L filter or an *LCL* filter is integrated between the inverter and the grid to reduce the total harmonic distortion of the injected currents (THDi). The advantages of the use of an *LCL* filter are the remarkable attenuation of switching harmonics, lower weight and size of the total hardware, and less cost-expensive with higher efficiency.

To control the waveform of the injected currents and the power factor precisely at the common coupling point with the grid, the grid-side currents are selected as the control variables [2], [3]. When the grid-side currents are the control targets, the *LCL*-filter resonance can make the closed-loop system unstable. To tackle the resonance different approaches are addressed in publications, which are mainly divided into active damping (AD) and passive damping (PD) [4], [5], [6], [7], [8]. Usually, AD needs an extra sensor for measuring a state variable of the system, which increases the total cost and reduces the reliability. PD adds a passive resistor in parallel or series with one element of the *LCL* filter and, thus, increases losses [9], [10].

From the other perspective, designing a high-performance control method that does not degrade the ability of the *LCL* filter to attenuate switching harmonics is necessary and is the aim of this research. This control has to remove the need for AD or PD and respects the requirements, such as high performance, zero steady-state offsets in tracking the sinusoidal references, robustness against the grid-inductance variations, and mismatches in the *LCL*-filter elements. A variety of control methods, such as sliding-mode control, deadbeat predictive control, and state-feedback control are developed for grid-tied inverters [3], [11], [12], [13], [14]. Basically, these control methods do not eliminate the need for AD or PD.

Model predictive control (MPC) has received overwhelming attention in industrial and academic societies in recent years [2]. MPC in power electronics is divided into two groups. The first group, which is called finite-control-set-MPC (FCS-MPC) solves an optimization problem in real time by considering the limited numbers of switching states of a power converter [15], [16], [17]. FCS-MPC has an excellent performance, which can be implemented for linear or nonlinear systems, but it does not remove the need for AD or PD [17], [18].

The second group is continuous-control-set-MPC (CCS-MPC). This method solves the optimization problem analytically and the control law is computed offline. The results are some simple numerical expressions in the continuous space. Contrary to FCS-MPC, the control voltages are realized with a modulator unit, and with a fixed-switching frequency and, thus,

Manuscript received 8 June 2023; revised 9 September 2023; accepted 8 October 2023. *(Corresponding author: Hasan Zamani.)*

Hasan Zamani is with K. N. Toosi University of Technology, Tehran 16317-14191, Iran, and also with BEAMS, Université libre de Bruxelles, 1050 Brussels, Belgium (e-mail: hasan.zamani@ulb.be).

Karim Abbaszadeh and Mohammad Hadi Karimi are with the Faculty of Electrical Engineering, K. N. Toosi University of Technology, Tehran 16317-14191, Iran (e-mail: abbaszadeh@kntu.ac.ir; mhkarimi@jdnasir.ac.ir).

Johan Gyselinck is with BEAMS, Université libre de Bruxelles, 1050 Brussels, Belgium (e-mail: johan.gyselinck@ulb.be).

Color versions of one or more figures in this article are available at https://doi.org/10.1109/TIE.2023.3325574.

Digital Object Identifier 10.1109/TIE.2023.3325574

lower THDi [19]. There are a few publications about CCS-MPC in power electronics and particularly for grid-tied inverters. In [20], [21], and [22], CCS-MPC is implemented for an L-filter inverter that is not confronted with the resonance issue, but the injected current has less quality than an *LCL* filter. The main difference between the algorithm in [22] and [20] or [21] is the way the reference currents in [22] is generated to control the active and reactive power for balanced and unbalanced grid voltages, while the reference currents in [20] and [21] are constant.

An *LC*-filter current-source converter is controlled by CCS-MPC in [5]. Its cost function contains the voltage of the filter capacitor as a state variable, which damps the resonance. The same configuration is implemented in [23] for a local resistive load that removes the need for AD. The inverter-side currents are the control variables of CCS-MPC for an *LCL*-filter inverter in [24] and [25]. Choosing the inverter-side currents as the control targets removes the need for resonance damping [2]. In [19] and [26], the grid-side currents together with the capacitor voltages of the *LCL* filter are included in the cost function of CCS-MPC. In [27], CCS-MPC is designed with a PD method to control the grid-side currents of a 4-leg *LCL*-filter inverter. In [28], there are two loops to control the grid-side currents. The outer loop controls the grid-side currents and a PI control is implemented. The inner loop controls the capacitor voltages and inverter-side currents with CCS-MPC. Therefore, two extra state variables are used and to reduce the number of sensors, a state estimator is designed and implemented.

As a summary, in the relevant papers for CCS-MPC, the stability against the *LCL*-filter resonance is guaranteed with either of the following two approaches: the inverter-side currents are the control targets, or their cost function includes some state variables. In each case, the state variables are measured by extra sensors or estimated by an observer, which increases the hardware cost and/or the control complexity.

In this article, it is shown that CCS-MPC has inherent robustness against the *LCL*-filter resonance and does not need extra sensors for AD. The other feature of CCS-MPC relies on its ability to track sinusoidal references in the stationary frame. The control is designed in the stationary frame because in the synchronous frame there are heavy cross-coupling terms between the *dq* axes and the order of the model is larger [18].

The control law of CCS-MPC contains past outputs, inputs, and the reference trajectory. It is shown that the past inputs and outputs in the control law guarantee robustness against the *LCL*-filter resonance, while considering the reference trajectory guarantees zero offsets in the tracking of sinusoidal references.

Inductance variation of a grid is a challenging issue in the *LCL*-filter grid-tied inverters, which arises instability. Even though CCS-MPC generally has good stability for parameter mismatches, the control law is optimized for the nominal value of the parameters. A relatively large variation may deteriorate the performance of the control and cause instability in the closed-loop system. To solve this problem, the controller parameters for a set of grid-side inductances are derived offline and a model for each coefficient of the control law is derived with a linear regression method. In simulation time or real time, the grid inductance is estimated with the method reported in [27] and the parameters in each condition are updated.

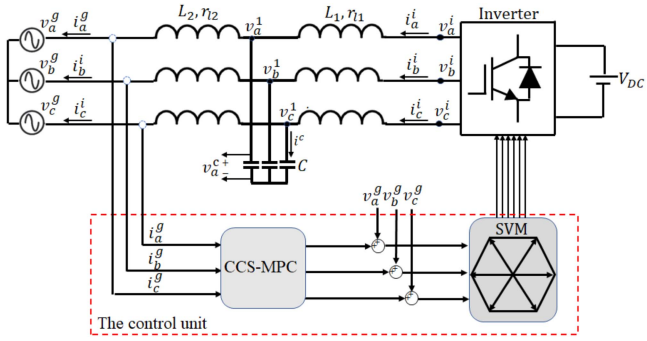

Fig. 1. Configuration of a three-phase *LCL* filter-based grid-tied inverter.

A summary of the proposed controller advantages is as follows.

1) The proposed MPC has inherent stability against the *LCL*-filter resonance, and extra sensors are avoided.
2) To handle large variations in the grid inductance, an adaptive CCS-MPC is proposed.
3) The optimization routine of the proposed control is performed offline and results are simple numerical expressions that can easily be implemented in low-cost processors.
4) Zero steady-state offset is guaranteed by parametrizing the control law and considering the reference trajectory during the control horizon.
5) To control the power factor precisely, the grid-side currents are selected as the control targets.
6) The parameters of the control are tuned via a sensitivity analysis including stability against grid-inductance variations.

The rest of this article is organized as follows. The system is modeled in Section II. In Section III, the concept of CCS-MPC is developed for *LCL*-filter grid-tied inverters, and the method to synthesize references in the stationary frame to control active and reactive currents is proposed. Also, the method to select parameters of the control based on the obtained transfer functions as well as the method to handle grid-side inductance variations are explained. To verify the controller performances, the simulation, and experimental results are given in Sections IV and V, respectively. Finally, Section VI concludes this article.

II. Modeling of the *LCL* Filter in the Stationary Frame

Fig. 1 shows a three-phase *LCL*-filter grid-tied inverter with L_1 is the inverter-side inductance, L_2 is the grid-side inductance, C is the capacitance of the *LCL* filter, $r_{1,2}$, and r_c are the parasitic equivalent series resistance (ESR) of the filter inductance and capacitance, respectively. Just the grid voltages and the grid-side currents are necessary to be sampled for the control. The ESRs are ignored in all simulation tests to evaluate the performance

TABLE I
INVERTER SPECIFICATIONS

Symbol	Quantity	Value
L_1	Inverter-side filter inductance	3 mH
L_2	Grid-side filter inductance	[1 12] mH
C	Filter capacitor	20 μF
r_{l1}, r_{l2}	Parasitic resistance of inductors	13 mΩ/mH
r_C	Parasitic resistance of capacitor	20 mΩ
v_{dc}	DC bus voltage	650 V
v^g	Grid voltage	380 Vrms
f_{sw}	Switching frequency	10 kHz
f_{res}	Resonance frequency	[726 1300] Hz
f	Grid frequency	50 Hz
S	Apparent power	5 kW

of adaptive CCS-MPC without any damping in the circuit. The design requirements of the *LCL* filter are [29], [30], [31] as follows.

1) The fundamental reactive power generation by the capacitors of the *LCL* filter should not exceed 10% of the rated apparent power S.
2) The fundamental voltage drop due to the grid-side and inverter-side inductances should not exceed 10% of the rated voltage. Otherwise, a higher dc-link voltage is required, which increases switching losses.
3) The resonance frequency of the *LCL* filter should be between 10 times the line frequency and half of the switching frequency.

Respecting the requirements, the *LCL*-filter parameters are listed in Table I . The capacitance is selected a little higher to evaluate the control robustness when the ESRs in the experiments cannot damp the resonance.

The dynamic equations of the system in the stationary reference frame are

$$v_x^i = r_{l1} i_x^i + L_2 \frac{di_x^i}{dt} + v_x^1 \tag{1}$$

$$v_x^1 = r_{l2} i_x^g + L_2 \frac{di_x^g}{dt} \tag{2}$$

$$i_x^c = C \frac{dv_x^c}{dt} \tag{3}$$

$$v_x^1 = v_x^c + r_c i_x^c \tag{4}$$

$$i_x^i = i_x^c + i_x^g \tag{5}$$

with $x \,\epsilon\, \{\alpha,\ \beta\}$, i and g are the superscripts for the inverter-side and the grid-side variables, v_x^1 is the voltage across the capacitor and its parasitic resistance. The transfer function relating the grid-side current and the inverter voltage with neglecting ESRs are

$$G_{\text{sys}}(s) = \frac{i_x^g}{v_x^i} = \frac{1}{L_2\, s} \frac{\gamma^2}{s^2 + \omega_{\text{res}}^2} \tag{6}$$

with the parameters given by

$$\omega_{\text{res}} = \sqrt{\frac{L_2 + L_1}{L_2 L_1 C}} \quad , \quad \gamma = \frac{1}{\sqrt{L_1 C}}. \tag{7}$$

To obtain $G_{\text{sys}}(s)$, the grid voltage is set to zero. A feed-forward term of the grid voltage to the control output can compensate for this simplification [25].

Formulation of CCS-MPC requires the controller autoregressive integral moving average (CARIMA) model of the system [32]

$$A(z^{-1})y(k) = z^{-d}B(z^{-1})u(k-1) + C(z^{-1})\frac{e(k)}{\Delta} \tag{8}$$

with z^{-1} is the backward Euler shift operator, $\Delta = 1 - z^{-1}$, y and u are the output and the input of the system, e is the variable, which models noise, and d is the input–output delay. A and B are polynomials in z^{-1} of order n_a and n_b, respectively

$$\begin{aligned} A\left(z^{-1}\right) &= 1 + a_1 z^{-1} + a_2 z^{-2} + \cdots + a_{n_a} z^{-n_a} \\ B\left(z^{-1}\right) &= b_0 + b_1 z^{-1} + b_2 z^{-2} + \cdots + b_{n_b} z^{-n_b}. \end{aligned} \tag{9}$$

Regarding the input–output delay, $d = 1$ is considered from here on. It is also further assumed white noise, so $C(z^{-1}) = 1$. Equation (6) is discretized with a 10 kHz sampling frequency for different values of L_2 in the interval of [1 12] mH, and different CARIMA models are derived. Then, the control law for each CARIMA model is extracted, regressors for spanning the space of the problem are selected, and models for each coefficient of the control are derived. These models are used in real time or simulation time and heavy computational requirements are avoided.

III. MODEL PREDICTIVE CONTROL

A. Derivation of CCS-MPC's Control Law

The control law of CCS-MPC is derived by solving the optimization problem for the cost function given by [32]

$$J = \sum_1^{N_f} \left|\left| \hat{y}(k+j)|k) - w(k+j) \right|\right|^2 + \lambda \sum_1^{N_c} \left|\left| \Delta u(k+j-1) \right|\right|^2 \tag{10}$$

with $\hat{y}(k+j)$ and $w(k+j)$ are the j-step ahead predicted output and the reference set point, $\Delta u(k)$ is the controller output variation, N_f, N_c, and λ are the prediction horizon, control horizon, and weighting factor, respectively. $\hat{y}(k+j|k)$ is used instead of $y(k+j)$ to explain that this variable is predicted (based on the past and future value of the system variables up to the instance k). In the following, N_c and N_f is assumed equal to N. Solving the optimization problem, (10) needs the prediction of outputs for the interval N, which can be obtained by solving the Diophantine equation:

$$1 = E_j\left(z^{-1}\right)\hat{A}\left(z^{-1}\right) + z^{-j}F_j\left(z^{-1}\right) \tag{11}$$

with $\hat{A} = \Delta A$, E_j, and F_j uniquely defined polynomials of degrees $j-1$ and n_a. They are obtained by dividing 1 by $\hat{A}$ for N steps. The remainder of each step is factorized as $z^{-j}F_j$, and the quotient of division is E_j. Multiplying (8) by $\Delta E_j z^j$ yields

$$\begin{aligned} &E_j\left(z^{-1}\right)\hat{A}\left(z^{-1}\right)y(k+j) \\ &= E_j\left(z^{-1}\right)B\left(z^{-1}\right)z^{-1}\Delta u(k+j) + E_j\left(z^{-1}\right)e(k+j). \end{aligned} \tag{12}$$

$e(k+j)$ relates to the future and is set to zero. Substitution of $E_j(z^{-1})\hat{A}$ from (11) in (12), and then leaving $y(k+j)$ in the

left-hand side and the other terms on the right-hand side, the prediction equation is obtained

$$\hat{y}(k+j \mid k) = G_j \Delta u(k+j-1) + F_j y(k) \tag{13}$$

with $G_j = E_j B$. There are recursive equations for the polynomials:

$$\begin{aligned} E_{j+1} &= E_j + z^{-j} f_{j,0} \\ f_{j+1,i} &= f_{j,i+1} - f_{j,0} \tilde{a}_{i+1} \quad i = 0 \cdots (n_a - 1) \\ G_{j+1} &= G_j + f_{j,0} z^{-j} B \end{aligned}$$

with $f_{j,i}$ is the ith coefficients of F_j, $\hat{a}_{i+1}$ is the $(i+1)$th coefficient of $\hat{A}$. The prediction equation contains both past signals and future signals. The matrix form of the prediction equation that separates the signals for $j = 1, \ldots, N$ is

$$Y = G_f U + F Y_p + G_p U_p \tag{14}$$

with

$$\begin{aligned} Y &= [\hat{y}(k+1|k), \hat{y}(k+2|k), \ldots, \hat{y}(k+N|k)]^T \\ Y_p &= [y(k), y(k-1), \ldots, y(k-n_a)]^T \\ U &= [\Delta u(k), \Delta u(k+1), \ldots, \Delta u(k+N-1)]^T \\ U_p &= [\Delta u(k-1), \Delta u(k-2), \ldots, \Delta u(k-n_b)]^T \end{aligned}$$

$$G_f = \begin{bmatrix} g_{0,0} & 0 & \cdots & 0 \\ g_{1,1} & g_{1,0} & \cdots & 0 \\ \vdots & \vdots & \vdots & \\ g_{N,N-1} & g_{N,N-2} & \cdots & g_{N,0} \end{bmatrix}$$

$$G_p = \begin{bmatrix} g_{0,1} & \cdots & g_{0,nb} \\ g_{1,2} & \cdots & g_{1,n_b+1} \\ \vdots & \vdots & \vdots \\ g_{N,N} & \cdots & g_{N,n_b+N} \end{bmatrix}, F = \begin{bmatrix} f_{0,0} & \cdots & f_{0,na} \\ f_{1,0} & \cdots & f_{1,na} \\ \vdots & \vdots & \vdots \\ f_{N,0} & \cdots & f_{N,n_a} \end{bmatrix} \tag{15}$$

with $g_{j,i}$ is the ith coefficient of G_j. $FY_p + G_p U_p$ in (14) only depends on the past and is called the free response. Equation (14) can be rewritten as

$$Y = G_f U + f \tag{16}$$

with $f = FY_p + G_p U_p$. The matrix form of the cost function using (16) in (10) is

$$J = (G_f U + f - W)^T (G_f U + f - W) + U^T \lambda U \tag{17}$$

with $W = [w(k+1), w(k+2), \ldots, w(k+N)]^T$. By setting the derivative of J with respect to U to zero, the control law is determined

$$U = (G_f^T G_f + \lambda I)^{-1} G_f^T (W - f) \tag{18}$$

with I is the identity matrix. U is a vector that contains control signals in the interval of $k = 0$ to $k = N$. In each sampling time, just $\Delta u(k)$ is selected and applied to the process

$$\Delta u = K(W - f) \tag{19}$$

with K is the first row of $(G_f^T G_f + \lambda I)^{-1} G_f^T$. There are recursive equations for the polynomials.

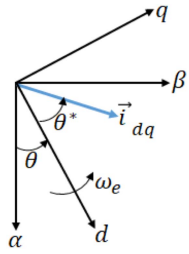

Fig. 2. Space vector of reference current in the synchronous and stationary reference frames. θ, which is the PLL output, is the angle between the α-axis and the d-axis. θ^* is the angle of $\vec{i}_{dq}$ in the synchronous *dq* frame.

B. References Synthesizing

To remove phase and amplitude offsets in the response of the control, the KW term in (19) is parameterized by considering the trajectory of references over the control horizon N. It is more convenient to set the references in the synchronous frame, and then convert them to the stationary frame. The space vector of the reference currents $\vec{i}_{dq}$ in the synchronous frame is

$$\vec{i}_{dq} = i_d^* + j i_q^* = I^* e^{j\theta^*} \tag{20}$$

with i_{dq}^* is the *dq* reference currents, I^* is the sum squared root of the *dq* reference currents, θ^* is the angle between $\vec{i}_{dq}$ and the d-axis. Fig. 2 shows all variables in the stationary and synchronous frames. I^* and θ^* are obtained as

$$I^* = \sqrt{i_{d^2}^* + i_{q^2}^*} \tag{21}$$

$$\theta^* = \arctan\left(\frac{i_q^*}{i_d^*}\right). \tag{22}$$

The electrical angle $\theta(k)$ between the α-axis and d-axis is supplied by a phase-locked loop (PLL). According to Fig. 2, θ^* is added to $\theta(k)$, and the angle of $\vec{i}_{dq}$ with respect to the α-axis is derived. Also, the evolution of θ at the time instant $k+i$ can be predicted as

$$\theta(k+i|k) = \theta(k) + i T_s \omega_e \tag{23}$$

with T_s is the sampling time, with fundamental frequency ω_e assumed constant. Therefore, the reference currents at $t = k+i$ are

$$i_\alpha^* = I^* \cos(\theta^* + \theta(k) + i T_s \omega_e) \tag{24}$$

$$i_\beta^* = I^* \sin(\theta^* + \theta(k) + i T_s \omega_e) \tag{25}$$

and the KW term becomes

$$\mathrm{KW}_{i_\alpha} = I^* \sum_{i=1}^{N} K(i) \cos(\theta^* + \theta(k) + i T_s \omega_e) \tag{26}$$

$$\mathrm{KW}_{i_\beta} = I^* \sum_{i=1}^{N} K(i) \sin(\theta^* + \theta(k) + i T_s \omega_e). \tag{27}$$

Adding a feed-forward term of the grid voltage to the control output reduces the injected current distortion due to grid voltage harmonics. i^g based on the superposition theorem for a simplified circuit where the *LCL* filter is approximated with an L

filter with $L = L_1 + L_2$, which is valid sufficiently below the resonance [33], can be written as

$$i^g = G_L v^i|_{v^g=0} - G_L v^g|_{v^i=0} \tag{28}$$

with $G_L = \frac{1}{Ls}$. It is assumed that the inverter is ideal, and the control output $u(k)$ is equal to the inverter output v^i ($v^i = u(k)$)

$$i^g = G_L(v^i + v^g) - G_L v^g = G_L v^i. \tag{29}$$

Equation (29) shows that with this modification, the injected current does not depend on the grid voltage and its harmonics.

C. Closed-Loop and Open-Loop Relationships

Once the control law is derived, it is possible to obtain the closed-loop poles. First, control law should be rewritten as negative orders of z. Using $f = FY_p + G_p U_P$ in (19) yields

$$\Delta u = \mathrm{KW} - KG_p U_P - KFY_p. \tag{30}$$

KG_pU_p can be rewritten as

$$KG_pU_p = K_u(z^{-1})\Delta u(k-1) \tag{31}$$

with $K_u(z^{-1})$ given by

$$K_u(z^{-1}) = \sum_{i=1}^{N} K_i g_{p_{i,0}} + \cdots + z^{-n_b} \sum_{i=1}^{N} K_i g_{p_{i,n_b}}$$

and KFY_p can be written as

$$KFY_p = K_y(z^{-1})y(k) \tag{32}$$

with $K_y(z^{-1})$ given by

$$K_y(z^{-1}) = \sum_{i=1}^{N} K_i f_{i,0} + \cdots + z^{-n_a} \sum_{i=1}^{N} K_i f_{i,n_a}.$$

Using (31) and (32) in (30) yields

$$\Delta u(k) = \mathrm{KW} - K_y\left(z^{-1}\right) y(k) - K_u\left(z^{-1}\right) \Delta u(k-1). \tag{33}$$

The future reference trajectory does not affect the characteristic equation. For the stability analysis, the reference set points in the interval N are kept constant, i.e., $w(k+j) = w(k)$, and KW becomes

$$r(k) = \mathrm{KW} = w(k) \sum_{i=1}^{N} K(i).$$

Substitution $r(k) = \mathrm{KW}$ in (33) and rearranging the equation yields

$$\Delta u(k) = T_1(z^{-1})r(k) - T_2\left(z^{-1}\right) y(k) \tag{34}$$

with $T_1(z^{-1})$ and $T_2(z^{-1})$ given by

$$T_1(z^{-1}) = \left(1 + z^{-1}K_u(z^{-1})\right)^{-1}$$

$$T_2(z^{-1}) = \left(1 + z^{-1}K_u(z^{-1})\right)^{-1} K_y(z^{-1}).$$

Using (34) in (8), the closed-loop transfer function $G_c(z^{-1})$ relating $y(k)$ and $r(k)$ is obtained

$$G_c\left(z^{-1}\right) = \frac{y(k)}{r(k)} = \left(A\Delta + Bz^{-1}T_2\right)^{-1} Bz^{-1}T_1. \tag{35}$$

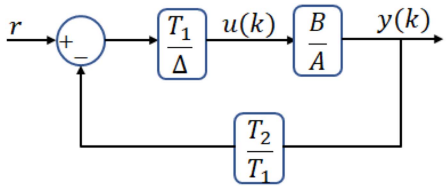

Fig. 3. Closed-loop structure of CCS-MPC.

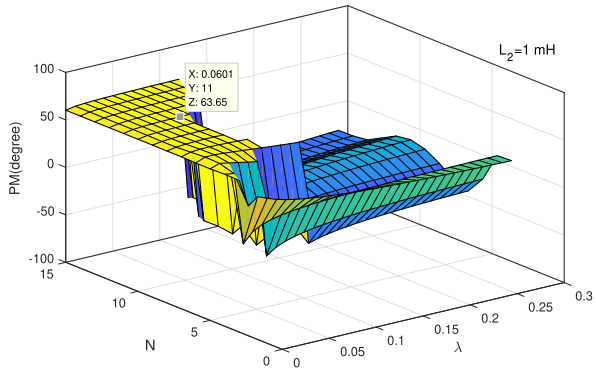

Fig. 4. PM and GM for L_2=1 mH when varying N and λ.

The denominator of (35) is the characteristic equation of the closed-loop system. The resulting closed-loop control scheme is shown in Fig. 3. The controller parameters are selected based on stability analysis of the open-loop transfer function $G_{\mathrm{op}}(z^{-1})$, which is derived by defining $\mathrm{err}(k) = r(k) - y(k)$ as the input and $y(k)$ as the output. Cross-multiplication of the first and third sides of (35) yields

$$y(k) = G_c\left(z^{-1}\right) r(k) \tag{36}$$

which results in

$$G_{\mathrm{op}}\left(z^{-1}\right) = \frac{y(k)}{r - y(k)} = \frac{G_c\left(z^{-1}\right)}{1 - G_c\left(z^{-1}\right)}. \tag{37}$$

D. Selection of the CCS-MPC Parameters

MPC parameters N and λ have a direct influence on the stability and the performance of the closed-loop system. To choose a value, the PM and GM of $G_{\mathrm{op}}(z^{-1})$ in (37) are studied. It is important to notice that the references in (26) and (27) are synthesized in real time and computation time increases with N. Therefore, the maximum value of GM and PM for the lowest value of N is searched. Figs. 4 to 7 shows PM and GM variations for L_2 =1 mH and 12 mH when varying N in the interval of [3 12] and λ in [0 0.3] Ω^{-2}. It is observed that the combination $N = 11$ and $\lambda = 0.06\,\Omega^{-2}$ fulfills the requirements. PM=63.65° and GM=6.02 dB for L_2 =1 mH, and PM=57.78° and GM=5.08 dB for L_2 =12 mH are marked in the figure for this set. $K_u(z^{-1})$ and $K_y(z^{-1})$ of the control law with L_2=1 mH and the selected parameters are

$$K_u\left(z^{-1}\right) = 0.302 + 0.063z^{-1}$$

$$K_y\left(z^{-1}\right) = 518 - 130.91z^{-1} + 128.08z^{-2} - 46.66z^{-3}.$$

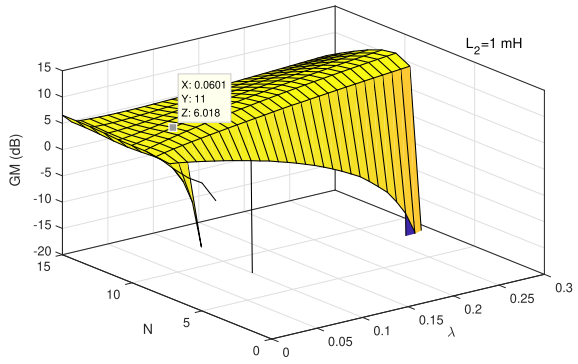

Fig. 5. PM and GM for L_2=1 mH when varying N and λ.

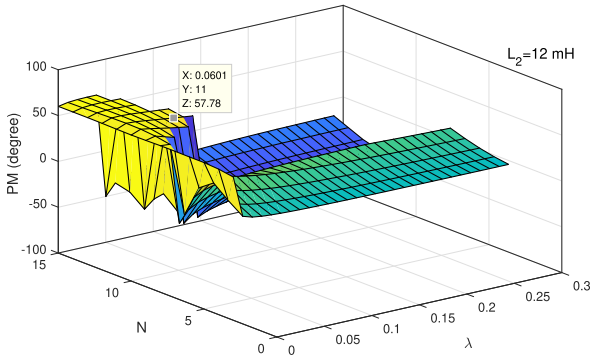

Fig. 6. PM and GM for L_2= 12 mH when varying N and λ.

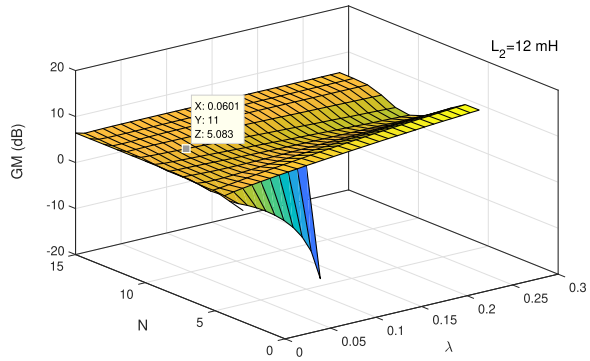

Fig. 7. PM and GM for L_2=12 mH when varying N and λ.

The control law includes a sequence of past outputs with the $K_y(z^{-1})$ polynomial and a sequence of past inputs with the $K_u(z^{-1})$ polynomial. The orders of $K_y(z^{-1})$ and $K_u(z^{-1})$ are equal to the order of the model's output and input polynomials [$A(z^{-1})$ and $B(z^{-1})$ in (8)], respectively. This shows that the proposed controller considers the internal interactions of the system and, hence, mitigates all harmonics with frequencies around the *LCL*-filter resonance and, thus, provides robustness against the resonance.

The CARIMA model is obtained for different values of the grid-side inductance in the interval of [1 12] mH with steps of 0.02 mH.

In each step, the same procedure for obtaining the control law is repeated, and the coefficients of $K_u(z^{-1})$ and $K_y(z^{-1})$ are

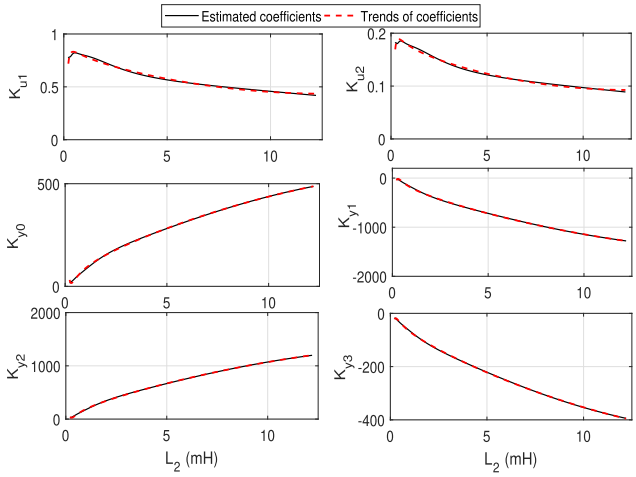

Fig. 8. Models for coefficients of $K_u(z^{-1})$ and $K_y(z^{-1})$.

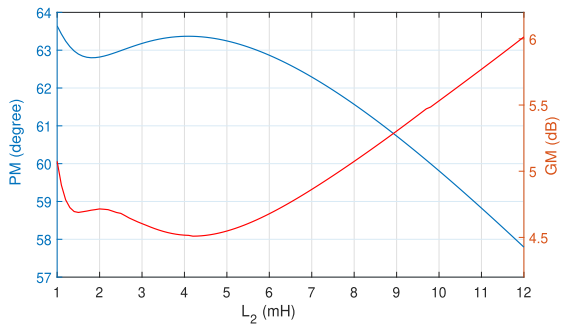

Fig. 9. PM and GM for N=11 and λ =0.06 Ω^{-2} as functions of L_2, the minimum values of PM and GM are 58 and 4.6 dB, respectively.

recorded. For each coefficient, a model is derived. After testing different models, it is turned out that the following regressors x_i can precisely span the space of the problem for all coefficients

$$x_1 = L_2,\ x_2 = 1/L_2,\ x_3 = 1/L_2^2$$

for a model given by

$$\hat{\phi} = X\theta \tag{38}$$

with $\hat{\phi}$ is the approximated model, θ is the parameter vector of the model, X is the regressor matrix given by

$$X = \begin{bmatrix} 1 & x_1 & x_2 & x_3 \end{bmatrix}. \tag{39}$$

θ is calculated by the ordinary least squares method [34]. The representative trends and their approximated model for the coefficients of $K_u(z^{-1})$ and $K_y(z^{-1})$ are plotted in Fig. 8. There are 11 models ($N = 11$) for K, which are not shown here. In real time or simulation time, the coefficients are adopted from these models according to the estimated grid-side inductance.

Fig. 9 shows variations of GM and PM when varying the grid-side inductances. The minimum GM in this interval is around 4.8 dB, and the minimum PM is 58°. With this strategy, the closed-loop system can remain stable for large variations of the grid inductance.

The influence of updating the control law for the stability of the closed-loop system is analyzed by the root loci of the

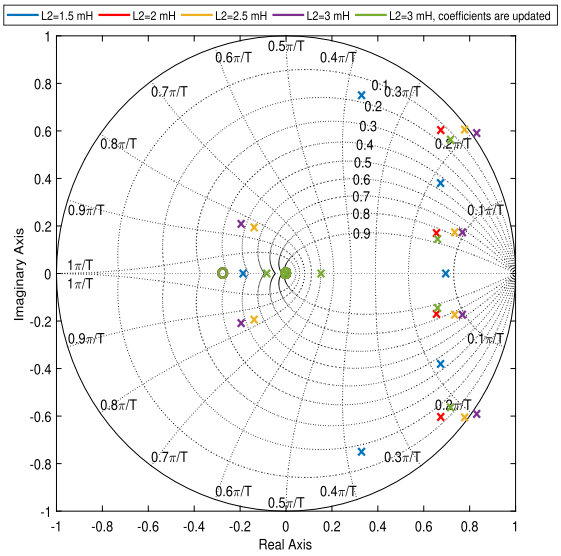

Fig. 10. Root locus in z-plane when varying the grid-side inductance.

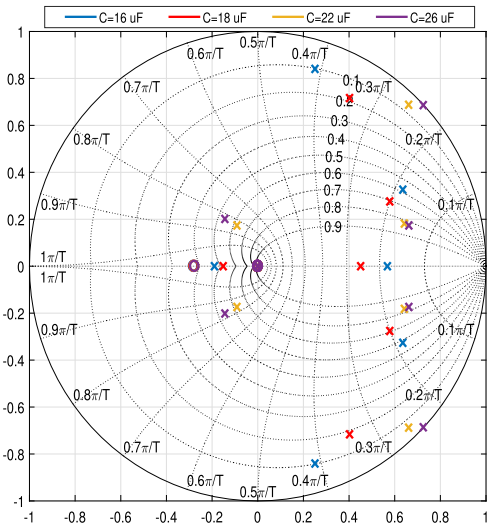

Fig. 11. Root locus in z-plane when varying the *LCL*-filter capacitance.

closed-loop transfer function [see (35)]. It is assumed that the parameters of the control law are initially selected for L_1 =3 mH, L_2 =2 mH, and C = 20 μF.

The grid-inductance variations can be studied by the variations in the grid-side inductance of the *LCL* filter. Fig. 10 shows the root loci for some values of L_2. For L_2 =1.5 mH, the closed-loop poles remain inside the unity circle and the system is stable. For L_2 equal to or larger than 2.5 mH, the system is unstable, and the inductance has to be estimated and the controller parameters updated. Doing so, the unstable poles return inside the unity circle. It is worth noting that no AD or PD is used.

To study the robustness of the proposed controller for the mismatch in parameters, the filter capacitance varies. Fig. 11 shows the root loci of the closed-loop poles. The system is stable for capacitance between 80% and 130% of the nominal value.

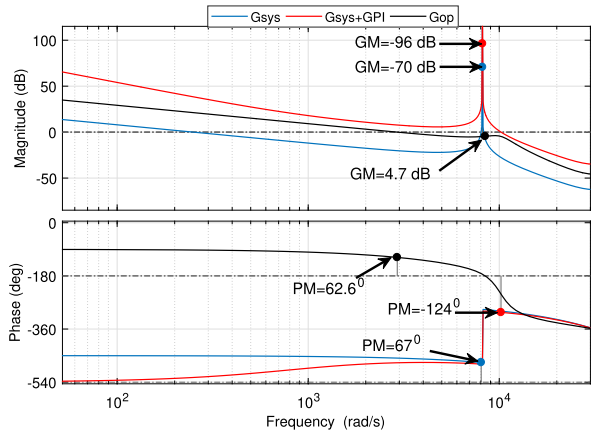

Fig. 12. Bode diagrams of the *LCL* filter, the open-loop system in the presence of the PI control, and CCS-MPC.

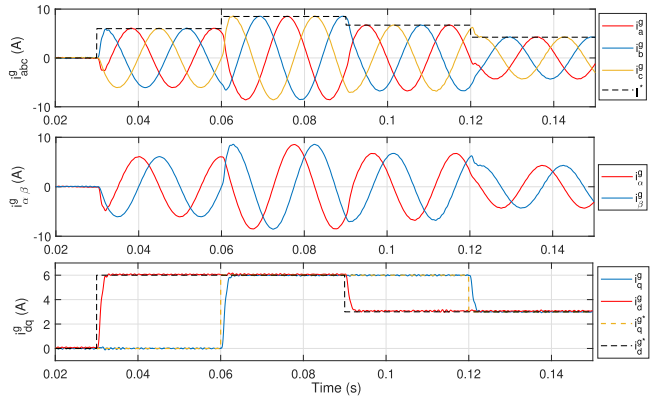

Fig. 13. Grid-side currents together with I^* in the abc frame and in the synchronous frame. The d-axis current at t=0.03 s, and the q-axis current at t =0.06 both are stepped up from 0 to 6 A, respectively, and stepped down at t =0.09 s and t = 0.12 from 6 to 3 A.

Equation (6) shows that G_{sys} is symmetrical for L_1 and L_2, and, therefore, variations of L_1 and L_2 have the same effect. Therefore, the given analysis for L_2 is valid when varying L_1.

Fig. 12 shows the Bode diagrams of $G_{\text{sys}}(s)$ in (6), the cascaded transfer function of $G_{\text{sys}}(s)$ and a PI controller, and $G_{\text{op}}(z^{-1})$ in (37). The PI controller gains are tuned with the symmetrical optimum method [35]. This figure shows that the GMs of $G_{\text{sys}}(s)$, and the open-loop system in the presence of the PI controller are negative, and therefore, the closed-loop systems are unstable. But GM and PM of $G_{\text{op}}(z^{-1})$ are both positive and provide a stable closed-loop system.

IV. Simulation Results

In these tests, a 2 mH grid-side inductance is used. The dq currents are converted to the $\alpha\beta$ frame and the KW terms of the control law are synthesized as explained in Section III-B. No AD or PD is used.

Fig. 13 shows the grid-side currents in the abc frame and in the synchronous frame, and I^* in (21). The d-axis current is stepped up at t= 0.03 s, and the q-axis current at t=0.06 s both from 0 to 6 A, and both stepped down from 6 to 3 A at t =0.09 s and

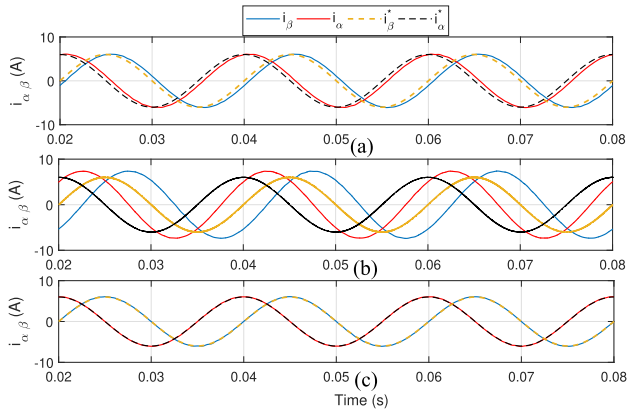

Fig. 14. Grid-side stationary currents in the steady-state condition. (a) Evolution of references during the control horizon is ignored. (b) Reference evolution and the grid voltage term are ignored. (c) Both terms are considered.

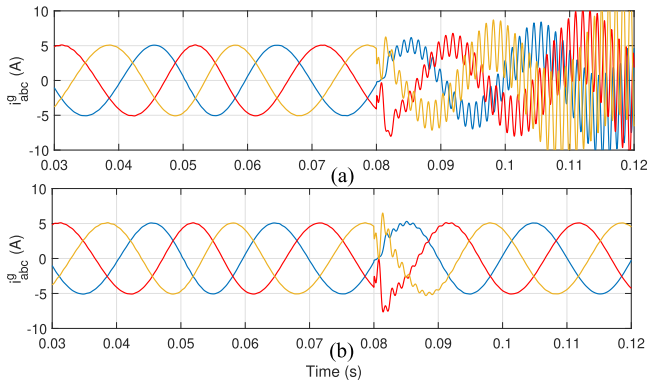

Fig. 15. Simulation results of the grid-side currents when the grid inductance is stepped up from 0 to 0.5 mH at $t = 0.05$ s, and from 0.5 to 2 mH at $t = 0.08$ s. (a) Control law is not updated. (b) Coefficients are updated for 4 mH.

$t = 0.12$ s, respectively. The amplitudes of the abc currents are limited to I^*, and the *dq* currents follow their references, which shows the proposed controller tracks sinusoidal references with zero steady-state offset. There is no oscillation in the response, which demonstrates the inherent robustness of the CCS-MPC against the *LCL*-filter resonance.

Fig. 14 shows the effects of considering the reference trajectory during the interval N and adding the grid voltage to the controller's output. When the evolution of the references is neglected, there is a phase offset in the response, the condition is worse when the evolution of references and the grid voltage term are ignored, and there is no offset either in phase or in the amplitude when both terms are considered.

The influence of updating the control law is studied with step changes in the grid inductance. The grid-side inductance of the *LCL* filter is 1.5 mH (the resonance frequency is $f_{\text{res}} = 1.12$ kHz) while the initial setting of the control coefficients are for 2 mH. The grid inductance is stepped up at t =0.05 s from 0 to 0.5 mH ($f_{\text{res}} = 1$ kHz) and stepped up from 0.5 mH to 2 mH ($f_{\text{res}} =$ 885 Hz) at t =0.08 s. Fig. 15 shows that the system starts oscillating and instability arises for the 2 mH grid inductance.

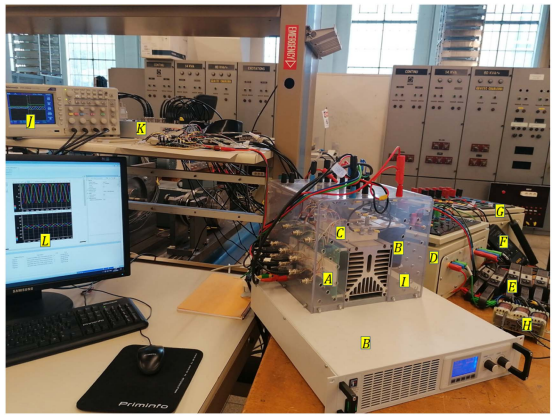

Fig. 16. Laboratory test bench with (A) IGBT drivers, (B) inverter dc-link capacitors, (C) IGBTs, (D) box of inductors, (E) current sensors, (F) voltage sensors, (G) box of ac capacitors, (H) extra inductors, (I) inverter, (J) oscilloscope, (K) dSPACE 1103, (L) ControlDesk.

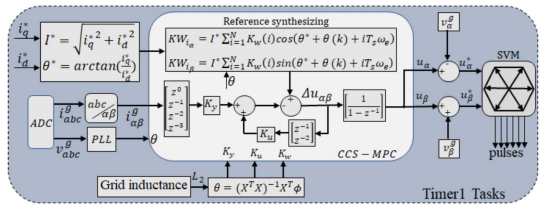

Fig. 17. Overall control unit implemented in a dSPACE 1103 prototype.

In the second test, the coefficients are updated and the system remains stable. The results are confirmed by the root locus analysis in Fig. 10.

V. Experimental Results

The proposed control method has been experimentally validated with the laboratory setup shown in Fig. 16. The two-level voltage source converter is a SEMIKRON Semiteach converter platform, based on the SKM50BG123D three-phase IGBT module. The dc-link capacitance is 1100 μF and is fed by a dc power supply. The implemented IGBT drivers are SKHI 22AR.

The grid-side currents are measured by three A622 current probes and the grid voltages by three P5200 HV high-voltage differential probes. Data are recorded with the TDS 2004 C Tektronix scope. The control has been implemented with a dSPACE 1103 fast prototype interface. The grid-side inductances are 3.0 mH with 5% tolerance. The filter capacitances are 20 μF.

The total control computation time of the CCS-MPC algorithm is around 12 μs and a considerable part of this time is dedicated to the reference synthesizing. The low computation time is expected because the optimization routine is performed offline. Fig. 17 shows the overall control algorithm, which is executed in Timer 1 with a 10 kHz sampling frequency. The grid-side inductance is estimated on site and the control law is updated.

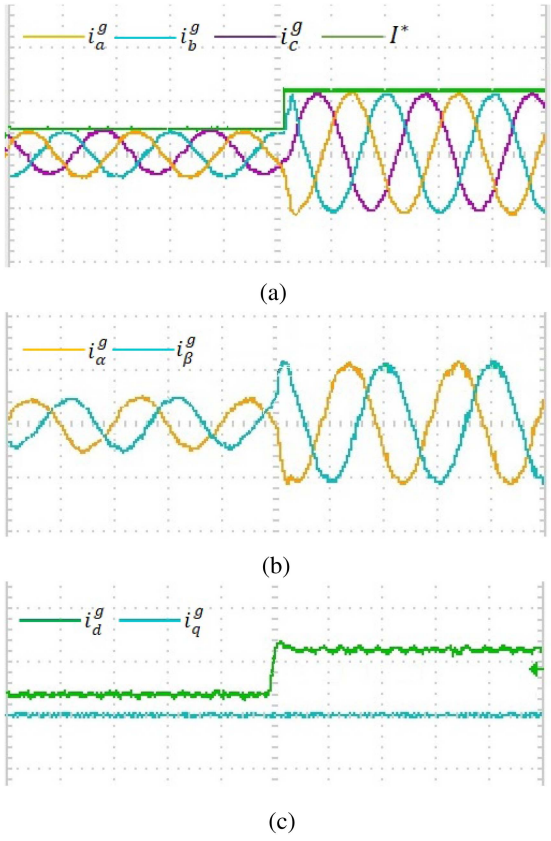

Fig. 18. Grid-side currents when the d-axis current is stepped up from 2 to 6 A and the q-axis reference current is kept constant at 0 A. (a) Grid-side currents and I^* in the abc frame (5 A/div). (b) Grid-side currents in the stationary $\alpha\beta$ frame (5 A/div). (c) Grid-side currents in the synchronous *dq* frame (5 A/div).

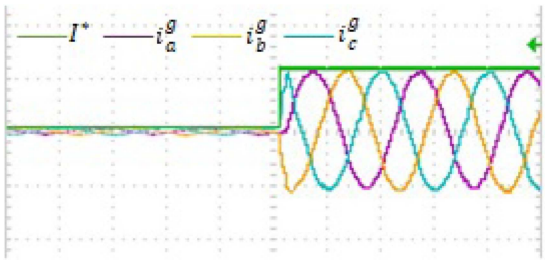

Fig. 19. Grid-side currents in the abc frame (5 A/div). The d-axis current is stepped up from 0 to 6 A and the q-axis current is set to 0 A.

In the first test, the d-axis reference current is stepped up from 2 to 6 A and the q-axis current is set to 0 A. Fig. 18 shows the grid-side currents in the abc, stationary, and synchronous frames. The W matrix is parameterized by considering the evolution of the reference in the control horizon N and the grid voltages are added to the controller's outputs. This figure shows that the proposed controller tracks the references with no offset neither in the amplitude nor in the phase. In addition, no oscillation is observed in the responses, which shows the inherent robustness of the proposed controller against the *LCL*-filter resonance. In another test, the step response of the control from the standstill

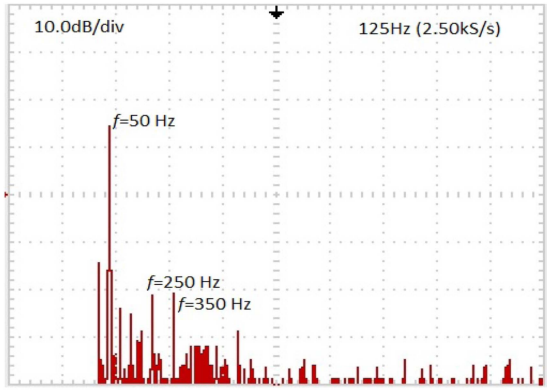

Fig. 20. Frequency spectrum of the a-phase grid-side current.

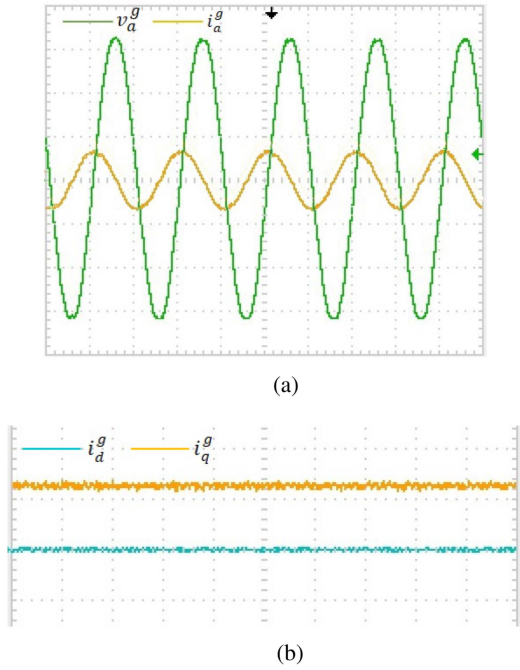

Fig. 21. d-axis reference current is set to 0 A, and the q-axis is set to 6 A. (a) a-phase grid-side current (10 A/div) and grid voltage (90 V/div). (b) Grid-side currents in the synchronous dq frame (5 A/div).

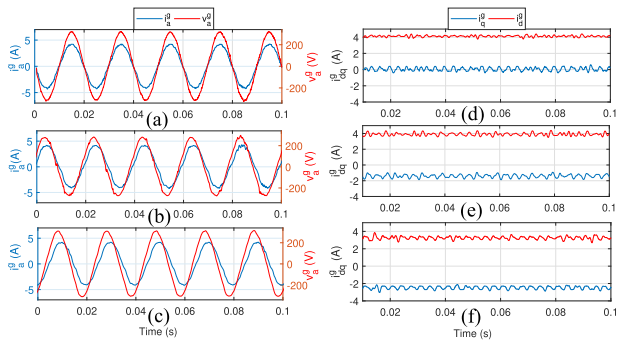

Fig. 22. a-phase grid-side current together with the grid voltage and the synchronous currents, (a) and (d) with considering the evolution of the reference currents during the interval N and adding the grid voltage to the control output, (b) and (e) with neglecting the evolution, (c) and (f) both terms are neglected.

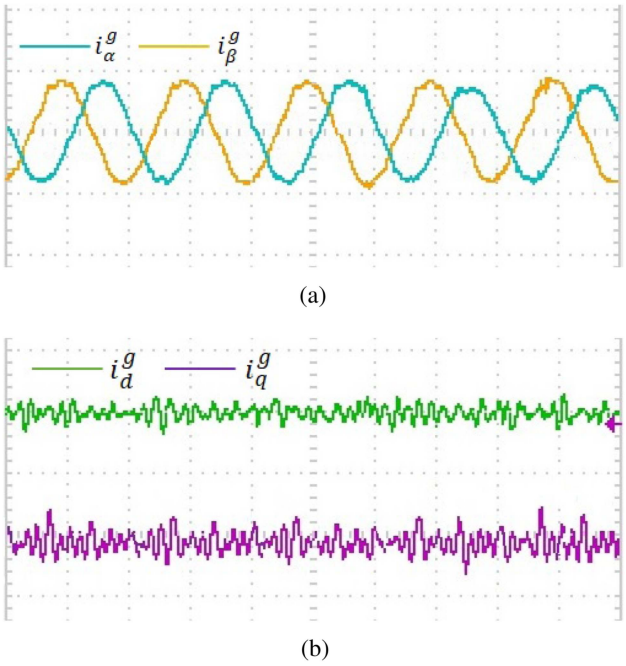

Fig. 23. Grid-side currents in the stationary and synchronous frames, the grid-side inductance is 1.2 mH. (a) Grid-side-currents in the stationary $\alpha\beta$ frame (5 A/div) with $L_2 = 1.2$ mH. (b) Grid-side currents in the synchronous *dq* frame (2 A/div).

is evaluated. Fig. 19 shows the results when the d-axis reference current is stepped up from 0 to 6 A and the q-axis reference current is 0 A. The references are well tracked and no oscillation is observed. This test ensures the controller's ability to inject current with a unity power factor, which is important in normal operation. Fig. 20 shows the a-phase grid-side current spectrum in the above test. The fifth and seventh harmonics are about 35 dB lower than the fundamental current. Therefore, the THDi is about 2%, which is in accordance with IEEE Std. 1547-2018.

The grid-tied inverter is requested to inject reactive currents during fault conditions to assist and improve the grid stability. In the next test, the q-axis reference current is set at 6 A and the d-axis reference current at 0 A. Fig. 21 shows the a-phase grid-side current and grid voltage. Also, the grid-side currents in the synchronous frame is shown. There is 90° phase shift between the current and voltage and the references are tracked with zero offsets.

The importance of considering the evolution of the references over the control horizon N as well as adding the grid voltages to the control output is analyzed in the next test. Fig. 22 shows the results for the following three scenarios.

Fig. 22(a) and (d): The grid voltages are added and the evolution of the references is considered. There is no offset in the response.

Fig. 22(b) and (e): The evolution is neglected, phase offset in the a-phase current, and 2 A amplitude offset in the response of the q-axis current are observed.

Fig. 22(c) and (f): Both terms are neglected. The condition is the worst, 2.5 A offset in the q-axis current and 0.5 A offset in the d-axis current appear and the currents are distorted. The tests could be repeated for 1.2 mH grid-side inductances. The d and q reference currents are set to 4 and 0 A, respectively. The control coefficients have to be updated. Otherwise, instability arises. Fig. 23 shows the stationary and synchronous currents in the steady-state condition. The control tracks the references with zero offsets and copes with the *LCL*-filter resonance.

VI. Conclusion

In this article, an adaptive CCS-MPC was designed for an *LCL*-filter grid-tied inverter in the stationary frame. Compared to the synchronous frame, the model complexity is lower and there is no coupling term between the axes.

It was shown that by parametrizing the control law with considering the trajectory of the references over the control horizon, CCS-MPC can track sinusoidal references, otherwise suffer from somewhat similar to other linear controllers. The parameters of the control were selected to provide the highest possible values of GM and PM for the lowest value of N.

The proposed controller showed inherent robustness against the *LCL*-filter resonance, which removes the need for an extra sensor for AD that increases the total cost, or a resistor for PD that increases losses.

The inductance variation of a grid is a challenging issue. It can shift the *LCL*-filter resonance frequency and cause instability. To solve this problem, an adaptive CCS-MPC was designed. The control coefficients were derived and for each coefficient a model was fitted by the linear regression method to avoid heavy real-time computational requirements. Then, they were updated in real time or simulation time according to the measured grid inductance.

Finally, it was shown that CCS-MPC is not a real-time computationally expensive algorithm.

References

[1] J. Roldan-Perez, E. J. Bueno, R. Pena-Alzola, and A. Rodríguez-Cabero, "All-pass-filter-based active damping for VSCS with LCL filters connected to weak grids," *IEEE Trans. Power Electron.*, vol. 33, no. 11, pp. 9890–9901, Nov. 2018, doi: 10.1109/TPEL.2017.2789218.

[2] R. Guzman, L. G. de Vicuña, M. Castilla, J. Miret, and J. de la Hoz,, "Variable structure control for three-phase LCL-filtered inverters using a reduced converter model," *IEEE Trans. Ind. Electron.*, vol. 65, no. 1, pp. 5–15, Jan. 2018.

[3] C. A. Busada, S. G. Jorge, and J. A. Solsona, "Full-state feedback equivalent controller for active damping in LCL-filtered grid-connected inverters using a reduced number of sensors," *IEEE Trans. Ind. Electron.*, vol. 62, no. 10, pp. 5993–6002, Oct. 2015.

[4] M. B. Said-Romdhane, M. W. Naouar, I. Slama-Belkhodja, and E. Monmasson, "Robust active damping methods for LCL filter-based grid-connected converters," *IEEE Trans. Power Electron.*, vol. 32, no. 9, pp. 6739–6750, Sep. 2016.

[5] O. Babayomi, Z. Zhang, T. Dragicevic, J. Hu, and J. Rodriguez, "Smart grid evolution: Predictive control of distributed energy resources a review," *Int. J. Elect. Power Energy Syst.*, vol. 147, 2023, Art. no. 108812.

[6] T. Fang, S. Shen, L. Zhang, Y. Jin, and C. Huang, "Capacitor current feedback with phase-lead compensator to eliminate resonant frequency forbidden region for LCL-type grid-connected inverter in weak grid," *IEEE Trans. Emerg. Sel. Topics Power Electron.*, vol. 9, no. 5, pp. 5581–5596, Oct. 2021.

[7] T. Liu, J. Liu, Z. Liu, and Z. Liu, "A study of virtual resistor-based active damping alternatives for LCL resonance in grid-connected voltage source inverters," *IEEE Trans. Power Electron.*, vol. 35, no. 1, pp. 247–262, Jan. 2019.

[8] D. Pan, X. Ruan, C. Bao, W. Li, and X. Wang, "Capacitor-current-feedback active damping with reduced computation delay for improving robustness of LCL-type grid-connected inverter," *IEEE Trans. Power Electron.*, vol. 29, no. 7, pp. 3414–3427, Jul. 2013.

[9] R. Pena-Alzola, M. Liserre, F. Blaabjerg, R. Sebastian, J. Dannehl, and F. W. Fuchs, "Analysis of the passive damping losses in LCL-filter-based grid converters," *IEEE Trans. Power Electron.*, vol. 28, no. 6, pp. 2642–2646, Jun. 2013.

[10] R. Beres, X. Wang, F. Blaabjerg, C. L. Bak, and M. Liserre, "Comparative evaluation of passive damping topologies for parallel grid-connected converters with LCL filters," in *Proc. Int. Power Electron. Conf.*, 2014, pp. 3320–3327.

[11] R. Guzman, L. G. De Vicuna, M. Castilla, J. Miret, and H. Martin, "Variable structure control in the natural frame for three-phase grid-connected inverters with LCL filter," *IEEE Trans. Power Electron.*, vol. 33, no. 5, pp. 4512–4522, May 2018.

[12] W. Jiang, W. Ma, J. Wang, L. Wang, and Y. Gao, "Deadbeat control based on current predictive calibration for grid-connected converter under unbalanced grid voltage," *IEEE Trans. Ind. Electron.*, vol. 64, no. 7, pp. 5479–5491, Jul. 2017.

[13] S. R. Mohapatra and V. Agarwal, "Model predictive controller with reduced complexity for grid-tied multilevel inverters," *IEEE Trans. Ind. Electron.*, vol. 66, no. 11, pp. 8851–8855, Nov. 2019.

[14] R. K. Subroto, C. H. Tsai, K. L. Lian, and H. Karimi, "Active resonance damping for an ultra weak grid-connected voltage source inverter with LCL filter based on an optimization and sliding mode control," in *Proc. IEEE/IAS 58th Ind. Commercial Power Syst. Tech. Conf.*, 2022, pp. 1–10.

[15] S. Jain, M. B. Shadmand, and R. S. Balog, "Decoupled active and reactive power predictive control for PV applications using a grid-tied quasi-z-source inverter," *IEEE Trans. Emerg. Sel. Topics Power Electron.*, vol. 6, no. 4, pp. 1769–1782, Dec. 2018.

[16] X. Chen, W. Wu, N. Gao, H. S.-H. Chung, M. Liserre, and F. Blaabjerg, "Finite control set model predictive control for LCL-filtered grid-tied inverter with minimum sensors," *IEEE Trans. Ind. Electron.*, vol. 67, no. 12, pp. 9980–9990, Dec. 2020.

[17] P. Karamanakos, M. Nahalparvari, and T. Geyer, "Fixed switching frequency direct model predictive control with continuous and discontinuous modulation for grid-tied converters with LCL filters," *IEEE Trans. Control Syst. Technol.*, vol. 29, no. 4, pp. 1503–1518, Jul. 2021.

[18] H. Zamani, K. Abbaszadeh, J. Gyselinck, and M. Karimi, "Robust continuous control set model predictive control in synchronous reference frame for grid-tied inverters," *IEEE J. Emerg. Sel. Topics Ind. Electron.*, vol. 4, no. 1, pp. 209–218, Jan. 2023, doi: 10.1109/JESTIE.2022.3183474.

[19] M. Rossi, P. Karamanakos, and F. Castelli-Dezza, "An indirect model predictive control method for grid-connected three-level neutral point clamped converters with LCL filters," *IEEE Trans. Ind. Appl.*, vol. 58, no. 3, pp. 3750–3768, May/Jun. 2022.

[20] R. Errouissi, S. Muyeen, A. Al-Durra, and S. Leng, "Experimental validation of a robust continuous nonlinear model predictive control based grid-interlinked photovoltaic inverter," *IEEE Trans. Ind. Electron.*, vol. 63, no. 7, pp. 4495–4505, Jul. 2016.

[21] M. G. Judewicz, S. A. Gonzalez, N. I. Echeverría, J. R. Fischer, and D. O. Carrica, "Generalized predictive current control (GPCC) for grid-tie three-phase inverters," *IEEE Trans. Ind. Electron.*, vol. 63, no. 7, pp. 4475–4484, Jul. 2016.

[22] P. Šimek, M. Bejvl, and V. Valouch, "Power control for grid-connected converter based on generalized predictive current control," *IEEE Trans. Emerg. Sel. Topics Power Electron.*, vol. 10, no. 6, pp. 7072–7083, Dec. 2022.

[23] S. Vazquez, C. Montero, C. Bordons, and L. G. Franquelo, "Design and experimental validation of a model predictive control strategy for a VSI with long prediction horizon," in *Proc. IEEE IECON 39th Annu. Conf. Ind. Electron. Soc.*, 2013, pp. 5788–5793.

[24] M. G. Judewicz, S. A. Gonzalez, J. R. Fischer, J. F. Martnez, and D. O. Carrica, "Inverter-side current control of grid-connected voltage source inverters with LCL filter based on generalized predictive control," *IEEE Trans. Emerg. Sel. Topics Power Electron.*, vol. 6, no. 4, pp. 1732–1743, Dec. 2018.

[25] R. Guzman, L. G. de Vicua, A. Camacho, J. Miret, and J. M. Rey, "Receding-horizon model-predictive control for a three-phase VSI with an LCL filter," *IEEE Trans. Ind. Electron.*, vol. 66, no. 9, pp. 6671–6680, Sep. 2019.

[26] C. Xue, D. Zhou, and Y. Li, "Hybrid model predictive current and voltage control for LCL-filtered grid-connected inverter," *IEEE Trans. Emerg. Sel. Topics Power Electron.*, vol. 9, no. 5, pp. 5747–5760, Oct. 2021.

[27] R. Pena-Alzola, M. Liserre, F. Blaabjerg, M. Ordonez, and T. Kerekes, "A self-commissioning notch filter for active damping in a three-phase LCL-filter-based grid-tie converter," *IEEE Trans. Power Electron.*, vol. 29, no. 12, pp. 6754–6761, Dec. 2014.

[28] L. Zhou and M. Preindl, "Optimal tracking and resonance damping design of cascaded modular model predictive control for a common-mode stabilized grid-tied LCL inverter," *IEEE Trans. Power Electron.*, vol. 37, no. 8, pp. 9226–9240, Aug. 2022.

[29] M. Dursun and M. K. Döşoğlu, "LCL filter design for grid connected three-phase inverter," in *Proc. 2nd Int. Symp. Multidisciplinary Stud. Innov. Technol.*, 2018, pp. 1–4.

[30] D. Solatialkaran, "Optimal output filter design for grid-tied inverters with GaN-based switching devices," Ph.D. dissertation, School of Information Technology and Electrical Engineering, The University of Queensland, St Lucia, QLD, Australia, 2021.

[31] M. Liserre, F. Blaabjerg, and S. Hansen, "Design and control of an LCL-filter-based three-phase active rectifier," *IEEE Trans. Ind. Appl.*, vol. 41, no. 5, pp. 1281–1291, Sep./Oct. 2005, doi: 10.1109/TIA.2005.853373.

[32] E. F. Camacho and C. B. Alba, *Model Predictive Control*. Berlin, Germany: Springer, 2013.

[33] S. G. Parker, B. P. McGrath, and D. G. Holmes, "Regions of active damping control for LCL filters," *IEEE Trans. Ind. Appl.*, vol. 50, no. 1, pp. 424–432, Jan./Feb. 2014.

[34] O. Nelles, "Nonlinear system identification," *Meas. Sci. Technol.*, vol. 13, no. 4, pp. 646–646, 2002.

[35] J. Dannehl, C. Wessels, and F. W. Fuchs, "Limitations of voltage-oriented PI current control of grid-connected PWM rectifiers with LCL filters," *IEEE Trans. Ind. Electron.*, vol. 56, no. 2, pp. 380–388, Feb. 2009.

Hasan Zamani He was born in Kashan, Iran, in 1985. He received the B.S. degree in electrical engineering from Isfahan University, Isfahan, Iran, in 2007 and the M.S. degree in power electronics within electrical motor drives from Qazvin International University, Qazvin, Iran, in 2010. He is currently working toward the Ph.D. degree with K. N. Toosi University, Tehran, Iran, and Universite Libre de Bruxelles, Bruxelles, Belgium. His research subject is Control of Grid-Tied inverters for renewable energy applications.

His current research interests include power electronics and control, which include ac machine AC-DC, DC-AC and DC-DC converters, and digital-signal-processing-based control applications.

Karim Abbaszadeh received the B.S. degree in communication engineering from the K. N. Toosi University of Technology, Tehran, Iran, in 1994 and the M.S. and Ph.D. degrees in electrical engineering from the Amir Kabir University of Technology, Tehran, Iran, in 1997 and 2000, respectively.

He joined from 2001 to 2003, as a Visiting Scholar with Texas A&M University, College Station, TX, USA. He is currently a Professor with the Electrical Engineering Department, K. N. Toosi University, Tehran, Iran. He has authored more than 70 published journal papers in these fields. He is actively involved in presenting short courses and consulting in his area of expertise in various industries. His main research interests and experience include Electrical machines, such as optimum design and fault diagnostic also power electronics, sensorless variable-speed drives, and multiphase variable-speed drives for traction analysis and propulsion applications.

Mohammad Hadi Karimi He was born in Tehran, Iran, in 1984. He received the B.S. degree in electrical engineering from Isfahan University, Isfahan, Iran, in 2007 and the M.S. degree in power electronics and electrical machines engineering from the K. N. Toosi University of Technology, Tehran, in 2010.

He was with the Power Electronics Laboratory, K. N. Toosi University and is currently a Researcher with the Academic Center for Education, Culture, and Research, K. N. Toosi University of Technology. His current research interests include power electronics and control, which include ac machine drives, and digital-signal-processing-based control applications.

Johan Gyselinck (Member, IEEE) received the M.Sc. and Ph.D. degrees in electromechanical engineering from Ghent University, Ghent, Belgium, in 1991 and 2000, respectively.

From 2000 to 2004, he was a Postdoctoral Researcher and avLecturer with the University of Liege, Liege, Belgium. Since 2004, he has been a Professor with the Universite Libre de Bruxelles, Bruxelles, Belgium. He is coauthor of some 300 journal and conference papers. His main teaching and research topics are low-frequency magnetics (finite-element and analytical modeling, numerical methods), electrical machines and drives (modeling, simulation, design, and experimental work), and renewables (wind and photovoltaics).